Supplementary Information

A Brain Tumor Molecular Imaging Strategy Using A New Triple-Modality MRI-Photoacoustic-Raman Nanoparticle

Moritz F. Kircher, Adam de la Zerda, Jesse V. Jokerst, Cristina L. Zavaleta, Paul J. Kempen, Erik Mittra, Ken Pitter, Ruimin Huang, Carl Campos, Frezghi Habte, Robert Sinclair, Cameron W. Brennan, Ingo K. Mellinghoff, Eric C. Holland and Sanjiv S. Gambhir

Corresponding Author: Sanjiv S. Gambhir, MD, PhD
The James H Clark Center
318 Campus Drive
Stanford, CA 94305-5427
E-mail: sgambhir@stanford.edu

A. Supplementary Data

Serum stability of Photoacoustic signal

To verify the stability of the optical absorbance of the MPRs in serum, MPRs were added to 50% mouse serum / 50% PBS (total volume 1 mL, MPR concentration 13 pM). We monitored the optical absorbance of the solution at 532 nm at multiple time points for 22 h **(Supplementary Figure 1)**. Control solution included 50% serum only. The optical absorbance of the control serum vial had increased slightly over the 22 h, likely due to the evaporation of water from the vial, leading to higher concentration of the serum. This effect has likely also occurred in the vial containing the MPRs in serum. However, subtracting the "serum only" absorbance from the "MPR in serum" absorbance shows a stable and consistent absorbance curve with a standard deviation from the mean average absorbance of 9.5%.

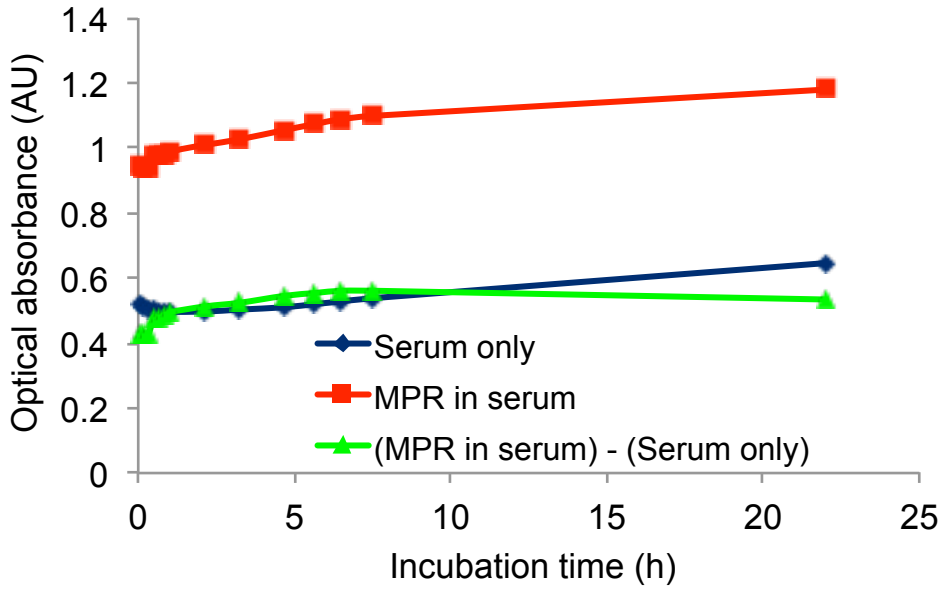

Supplementary Figure 1. Optical serum stability of MPRs. The MPRs showed a high level of optical stability when exposed to serum. Over the course of 22 h, the optical absorbance of a vial containing 50% serum only (blue curve) and a vial containing MPRs with 50% serum (red curve) were monitored. The blue and red curves show a slight increase of absorbance over time, an effect which is likely due to the evaporation of water from the vials, thereby increasing the concentration of serum in the vial. The green curve represents the subtraction of the "serum only" curve from the "MPR in serum" curve.

Stability of the hydrodynamic size during serum incubation

To validate the stability of the MPRs in serum, we measured the MPR's hydrodynamic size distribution using a dynamic light scattering instrument (Zetasizer, Malvern). The MPRs were added to 50% mouse serum / 50% PBS at a concentration of 0.068 nM and incubated at 37 °C for 24 h. The sample was analyzed at 0 h, 1 h, 2 h, 4 h, 6 h and 24 h post-incubation by dynamic light scattering. Over the course of 24 h, we noticed a slight increase in the hydrodynamic radius and the polydispersity index (PDI) of the MPRs (peaking at 1 h post-incubation with serum), which is attributed to association with blood proteins. In addition, a small peak was observed near 4,500 nm, attributed to aggregation; however, this peak was less than 5% of the total intensity for all measurements. Hence, we concluded that the MPRs are stable in serum (**Supplementary Fig. 2**).

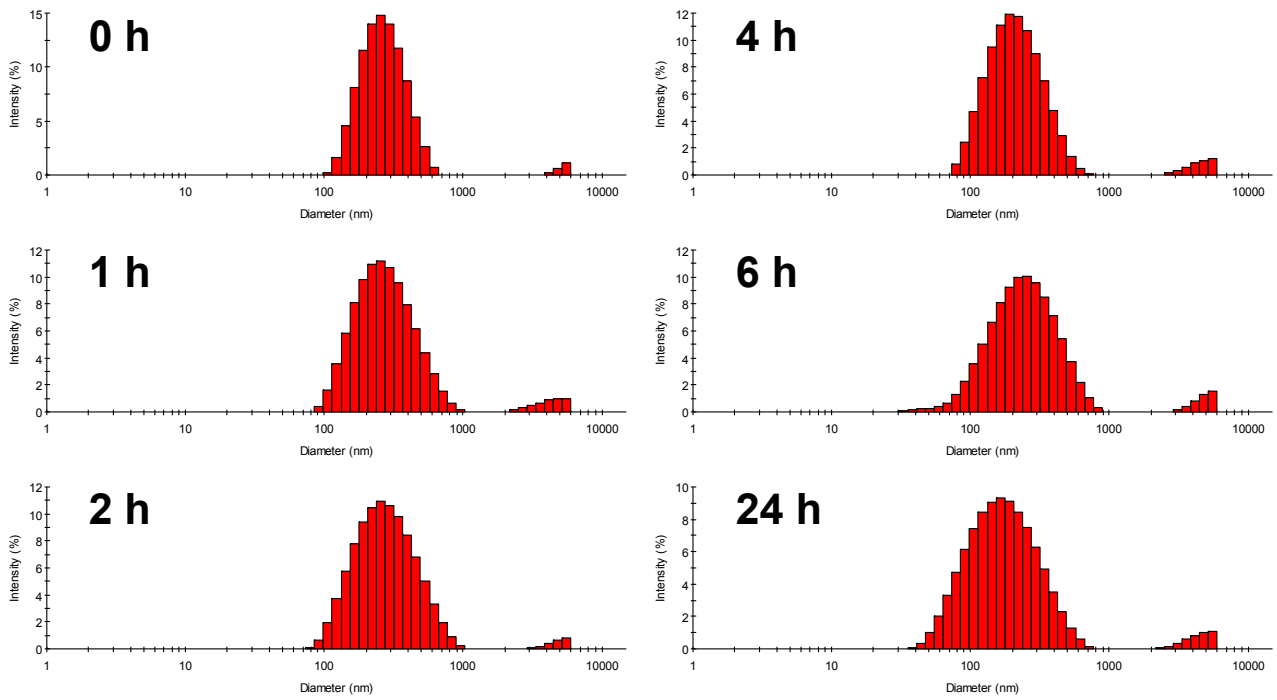

Supplementary Figure 2. Stability of the MPR hydrodynamic size during serum incubation. MPRs were incubated with 50% mouse serum / 50% PBS for 24 h at 37 ^{o}C. Hydrodynamic measurements of the samples taken with a dynamic light scattering instrument indicated that the particles' hydrodynamic size is stable over the course of 24 h of serum incubation.

Stability of Raman spectrum before vs. after maleimide-DOTA-Gd conjugation

We validated that the Raman spectrum of the MPRs is not affected by the surface conjugation procedure by acquiring the Raman spectrum of a sample before and after the conjugation with maleimide-DOTA-Gd. As illustrated in **Supplementary Figure 3**, the addition of maleimide-DOTA-Gd shows a negligible effect on the Raman spectrum.

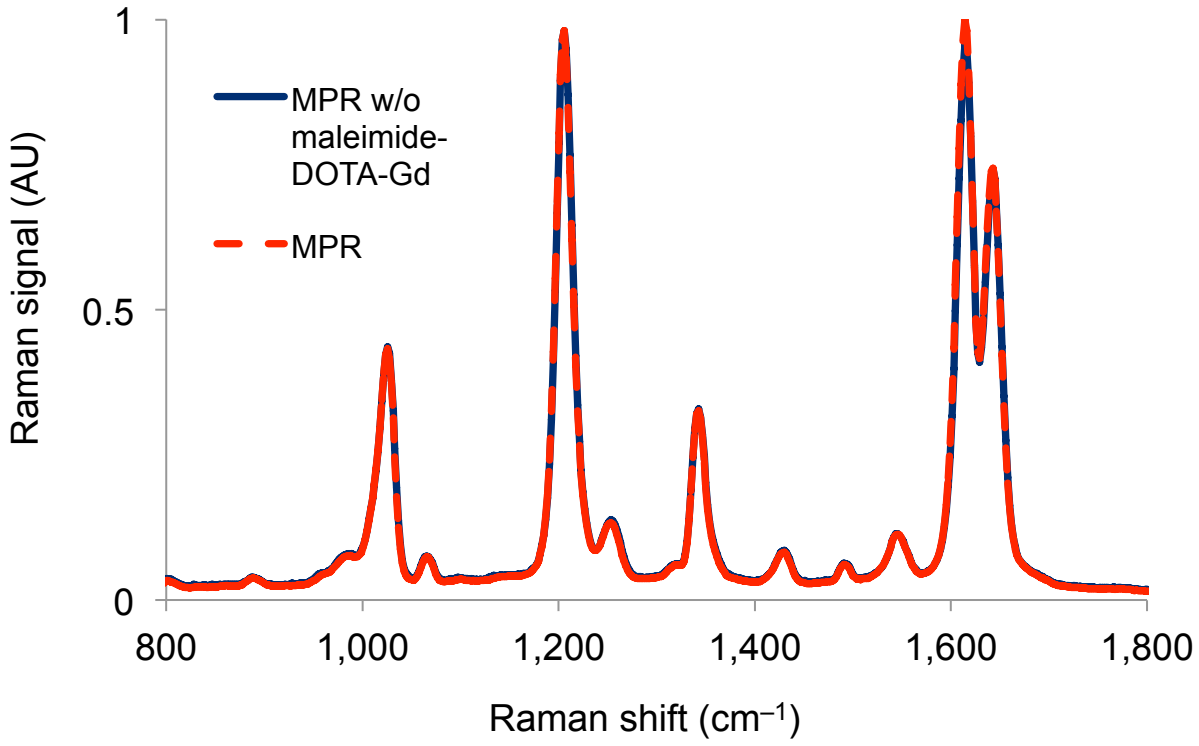

Supplementary Figure 3. Stability of Raman spectrum before vs. after maleimide-DOTA-Gd conjugation. Raman spectra of MPRs before (blue curve) and after (dashed red curve) conjugation of maleimide-DOTA-Gd are virtually identical.

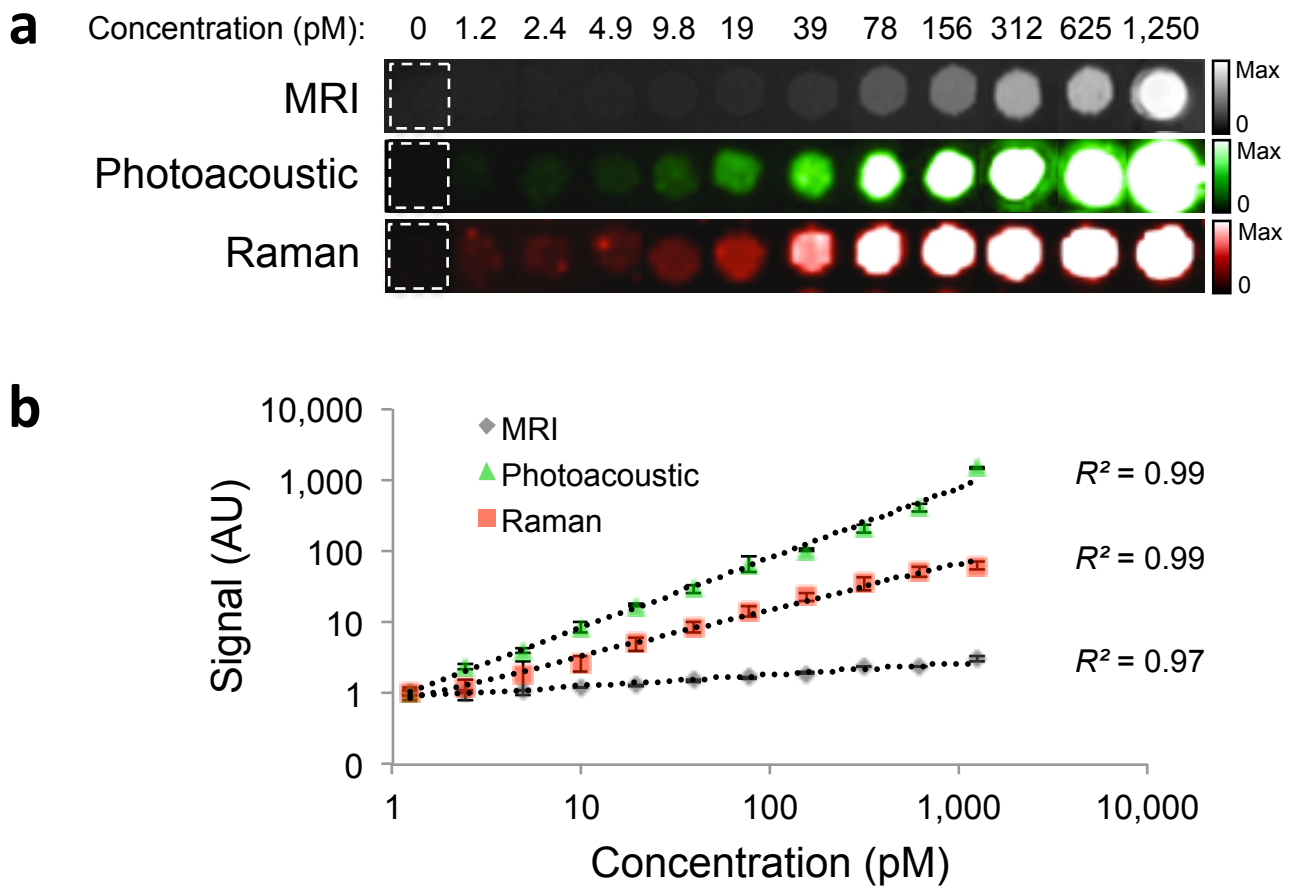

Supplementary Figure 4. Detection of MPRs *in vitro*. (**a**). An agarose phantom containing increasing concentrations of MPRs was scanned with MRI (upper row), Photoacoustic (middle row), and Raman (bottom row) instruments. The experiment was performed in triplicate. MRI was able to detect concentrations as low as 4.9 pM. The Photoacoustic and Raman imaging systems were able to detect even lower concentrations as low as 1.2 pM. (**b**) The MRI, Photoacoustic and Raman signals increased linearly with the MPR concentration (R^2 = 0.97, 0.99 and 0.99, respectively). Error bars represent s.e.m.

Raman *ex vivo* detection threshold

The phantom depicted in Supplementary Figure 4 was extended to include lower concentrations in order to determine the true Raman detection threshold (**Supplementary Fig. 5**). The detection threshold for Raman imaging in this new agarose phantom was determined to be approximately 610 fM.

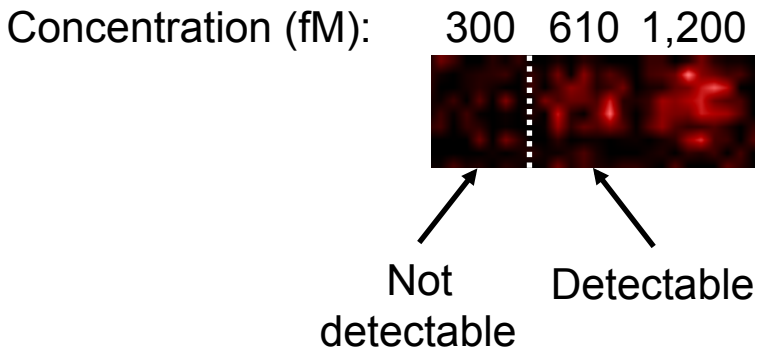

Supplementary Figure 5. Raman *ex vivo* detection threshold. The phantom shown in Supplementary Figure 4 was extended to two additional lower concentrations (300 and 610 fM) to demonstrate the true Raman detection threshold. The lowest concentration detectable was 610 fM (note that a different image scale was used here than in Supplementary Figure 4 to allow visualization of these low concentrations. Black color still represents true zero Raman signal.

Correlation of signal-concentration curves for MRI vs. Photoacoustic vs. Raman Imaging (in Phantom)

We further explored the correlation between the MRI signal-concentration response curve to the Photoacoustic signal-concentration response curve, to the Raman signal-concentration response curve in the phantom experiment (Supplementary Figure 4). For this purpose, we plotted 3 graphs: MRI vs. Photoacoustic, MRI vs. Raman and Raman vs. Photoacoustic (**Supplementary Figure 6**).

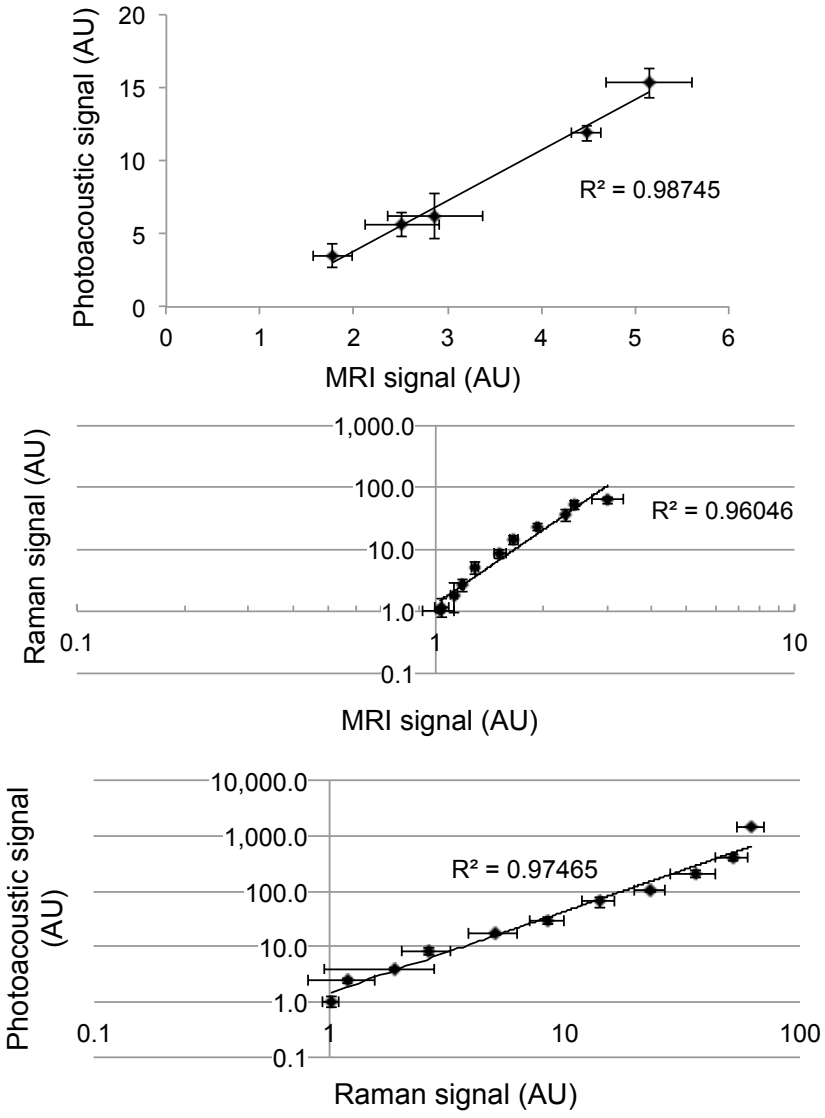

Supplementary Figure 6. Inter-modality signal correlation in phantom. MRI vs. Photoacoustic (top), MRI vs. Raman (middle), Raman vs. Photoacoustic (bottom).

Comparison of depth penetration – Photoacoustic versus Raman imaging

In order to compare the depth of penetration achieved by Photoacoustic imaging versus Raman imaging, we constructed a tissue-mimicking phantom containing MPRs at increasing depths. The phantom was based on an agarose gel to mimic the acoustic properties of soft tissues. India ink and liposyn were further added to the liquid agarose to mimic the optical absorption and optical scattering properties of biological tissues (**see Supplementary Methods**). The depths in the phantom were measured by an independent ultrasound image of the phantom which showed the location of the inclusions with respect to the upper surface of the phantom.

As **Supplementary Figure 7** shows, Photoacoustic imaging was able to detect signal from all wells of the phantom, i.e. depth of penetration is well beyond 7.1 mm. The deepest well Raman imaging was capable of visualizing was 4.5 mm in depth.

These results are highly dependent on the specific tissue optical properties (scattering and absorption alike). Specifically, white and gray matter exhibit different optical properties, which influence the depth of penetration. Hence, the values calculated here should only be interpreted as guidelines for relative rather than absolute penetration depth values.

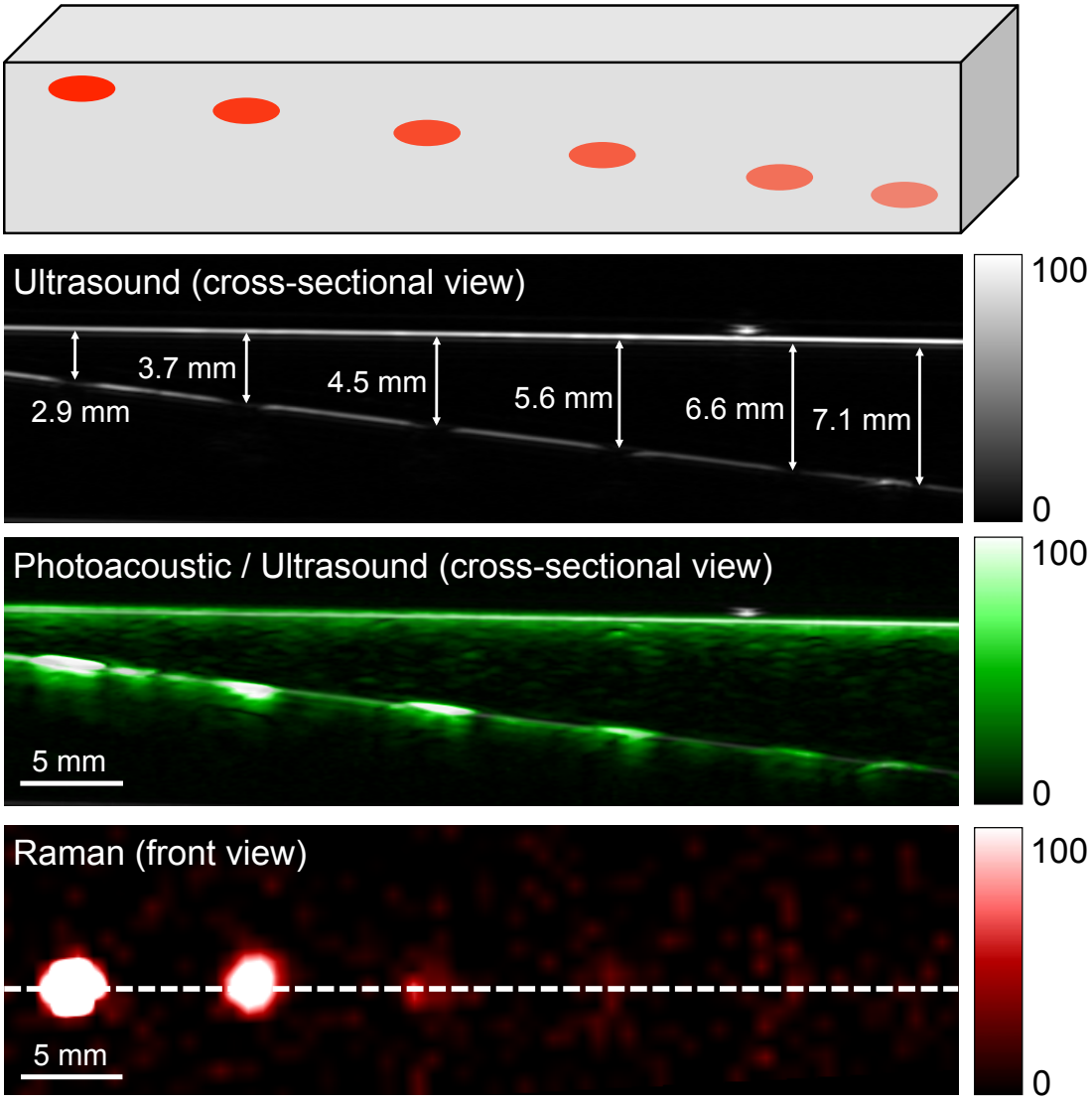

Supplementary Figure 7. Superiority of Photoacoustic imaging in visualizing deep objects. A tissue mimicking phantom with 6 inclusions containing MPRs at increasing depths (upper diagram) was scanned with ultrasound (grayscale), Photoacoustic (green color scale) and Raman (red color scale) imaging systems. The ultrasound image reveal the depth of the inclusions while the Photoacoustic and Raman images depict the imaging signal emitted by the MPRs. While the Photoacoustic image clearly visualized all 6 inclusions, the Raman imaging instrument was capable of visualizing only the first 3 inclusions, up to a depth of 4.5 mm. The white dashed line on the Raman image represents the location of the Photoacoustic and ultrasound cross sectional image slices. The color scale bars show relative signal.

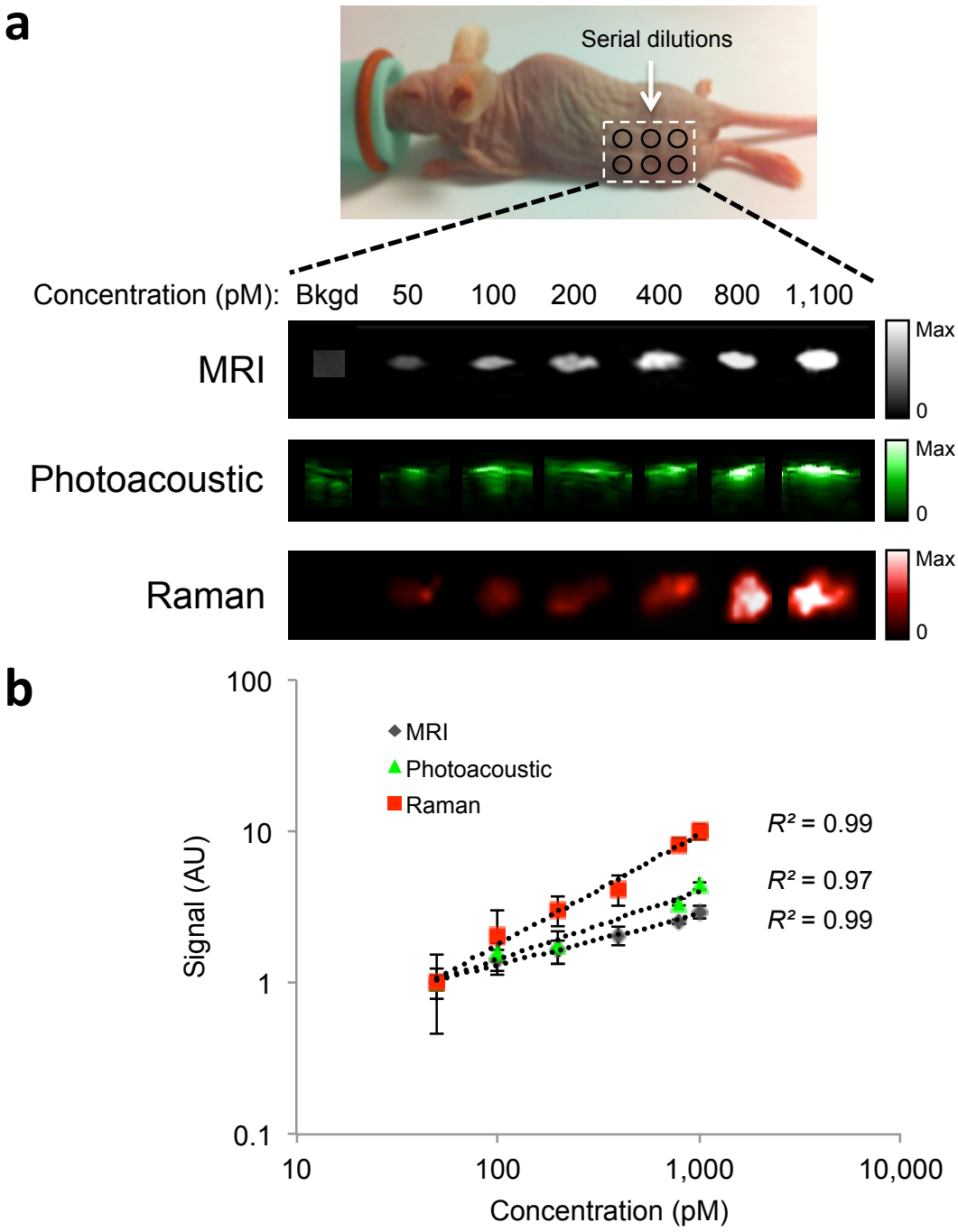

Supplementary Figure 8. Detection of MPRs in living mice. (**a**) MPRs ranging in concentrations from 50 pM to 1100 pM were injected subcutaneously into the flank of living mice (*n* = 3) and scanned with MRI, Photoacoustic and Raman instruments. MRI and Photoacoustic imaging clearly visualized the 100 pM concentration, while the 50 pM concentration showed signal close to the background (bkgd; muscle) level. The Raman image, however, clearly showed a distinct signal from the 50 pM well. (**b**) The MRI, Photoacoustic and Raman signals recorded *in vivo* increased linearly with the MPR concentration (R^2 = 0.99, 0.97 and 0.99 respectively). Error bars represent s.e.m.

Correlation of signal-concentration curves for MRI vs. Photoacoustic vs. Raman Imaging (*in vivo*)

We then explored the correlation between the MRI signal-concentration response curve to the Photoacoustic signal-concentration response curve, to the Raman signal-concentration response curve in the *in vivo* subcutaneous injection experiment (**Supplementary Figure 8**). A high degree of linearity was observed across all three modalities **(Supplementary Figure 9).**

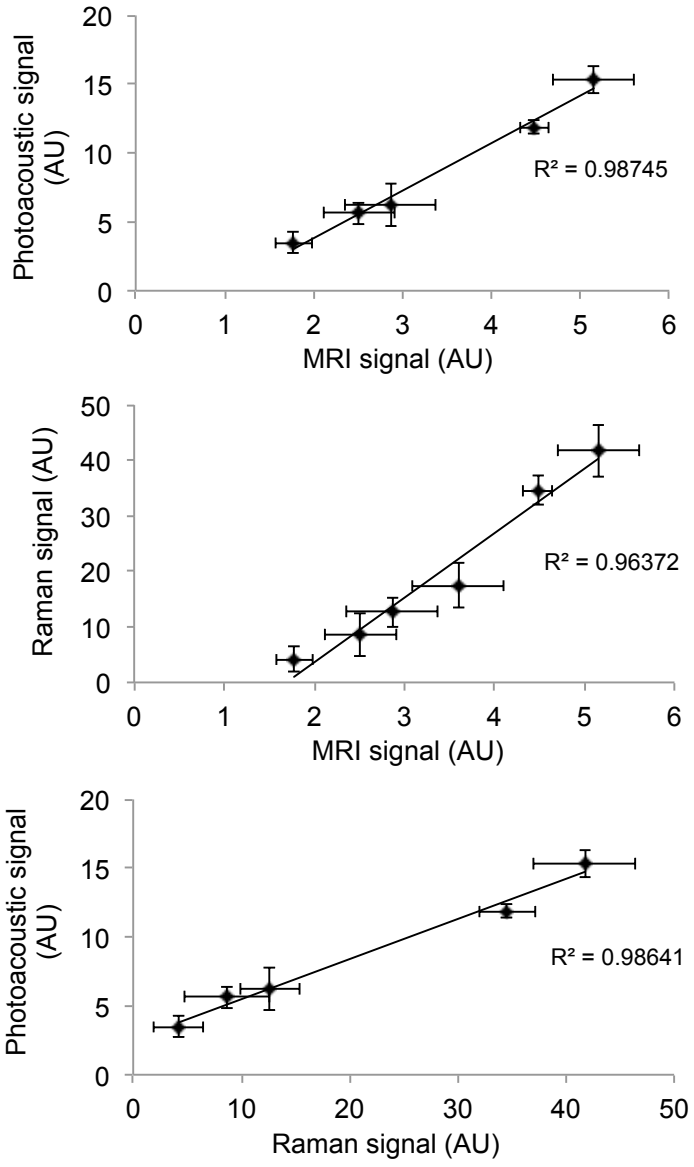

Supplementary Figure 9. Inter-modality signal correlation *in vivo*. MRI vs. Photoacoustic (top), MRI vs. Raman (middle), Raman vs. Photoacoustic (bottom).

Coronal reformation of the Photoacoustic-MRI overlay

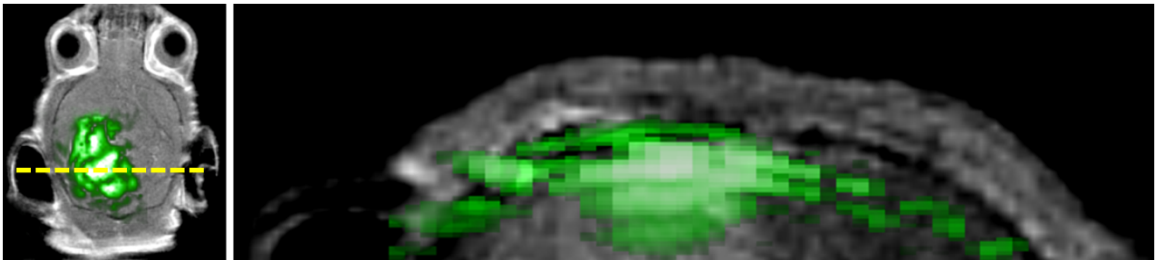

Supplementary Figure 10. Coronal reformation of the Photoacoustic-MRI overlay (taken from Figure 3), illustrating the three-dimensional nature of Photoacoustic imaging.

Dynamic triple-modality imaging

In order to determine the kinetics of the MPRs in all three modalities, we prepared additional eGFP^{+}U87MG orthotopic tumor-bearing mice (n = 4 for MRI and n = 4 for Raman imaging. The data for Photoacoustic imaging is derived from the same mice (n = 4) described in Figure 3 of the main text. A dose of 170 µL of 16 nM MPR suspension was injected intravenously into mice, and MRI, Photoacoustic, or Raman images were taken before the injection as well as 30 min, 60 min, 90 min and 120 min post-injection without moving the mice from the respective imaging instrument. The mice that were scanned using MRI underwent an additional 24 h post-injection MRI scan. As shown in **Supplementary Figure 11**, the MRI tumor contrast-to-noise ratio has increased significantly by 30 min post-injection and remained high throughout the 24 h period. The kinetics of the MPRs that were observed with the Photoacoustic system were very similar to that of MRI, further validating this behavior. Finally, the Raman signal showed a significant increase 30 min post-injection, and then dropped and stabilized at about half the value (**Supplementary Fig. 11**). This behavior can be explained by the fact that Raman imaging, unlike MRI or Photoacoustic imaging, is integrating the signal from all tissues under the surface into a 2D image. This includes the skin and healthy brain tissue in which the MPRs circulate but are not retained.

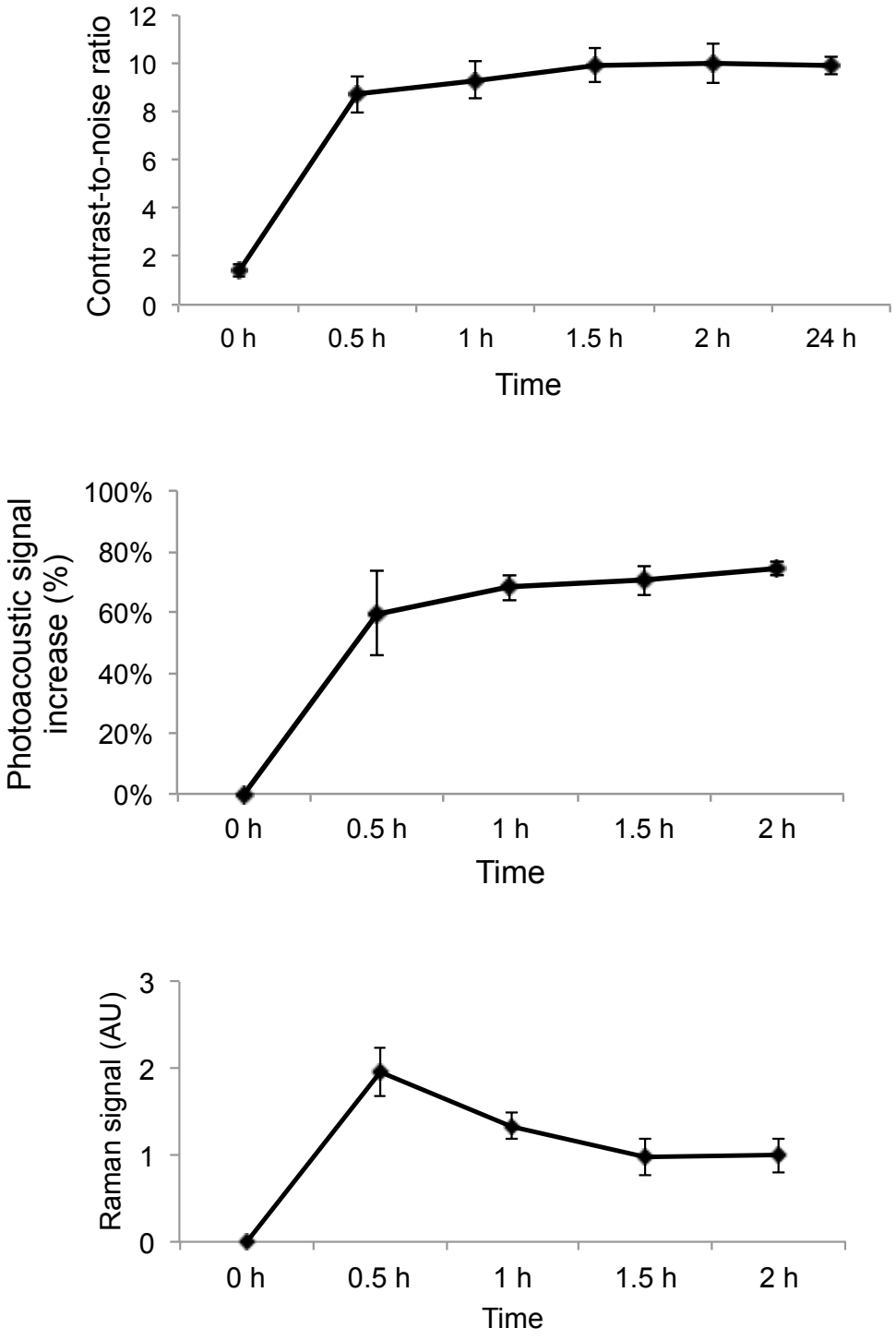

Supplementary Figure 11. MPR *in vivo* signal kinetics. Unlike the MRI (top) and Photoacoustic (middle) kinetic curves, the Raman (bottom) kinetic curve showed an initial peak at 0.5 h, followed by a decrease to a plateau at 1.5 h. This effect is presumably due to initial nonspecific circulation of MPRs in superficial layers, before clearance of MPRs from the blood-stream has occurred. Raman is most sensitive to superficial layers such as the skin because of the proximity of the lens to the skin surface of the animal. Error bars represent s.e.m.

Visualization of infiltrative tumor margins, finger-like protrusions, and isolated tumor foci

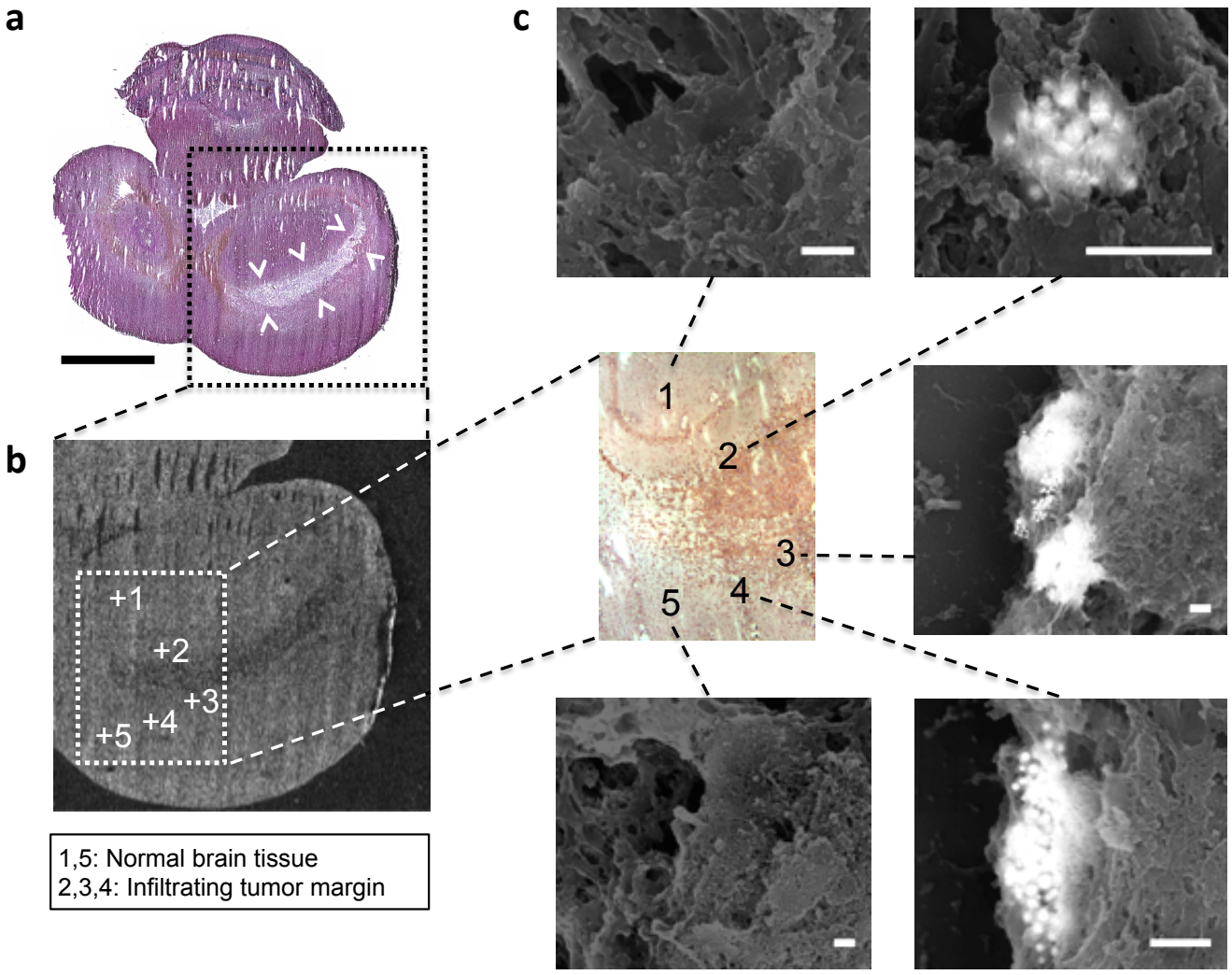

Supplementary Figure 12. MPRs accumulate in infiltrating tumor margins in an orthotopic primary human glioblastoma (GBM) xenograft mouse model. Tumor-bearing mice were injected intravenously with MPRs (150 µl, 16 nM, *n* = 4). At 24 h post-injection, brains were excised and cryosections (10 µm slice thickness) were stained with hematoxylin and eosin (H&E) and subsequently analyzed with a scanning electron microscope (SEM). Adjacent sections were stained with Olig2-specific immunohistochemistry (center image). (**a**) H&E stain of the brain showing a tumor in the right hemisphere (boxed region). (**b**) An SEM scan of this H&E section was then acquired to sample high magnification SEM images from precise locations of the tumor and surrounding brain parenchyma (exact sample locations indicated by '+' signs). (**c**) Higher magnification SEM images taken from five different locations in the brain were acquired (overlay of secondary electron SEM on backscattered electron SEM, MPRs shown as white dots). Location 1 and 5 represent normal brain tissue as confirmed by IHC, whereas locations 2-4 represent zones of infiltrating tumor margin. Note that many clusters of MPRs were found not only in the bulk tumor but indeed also in the diffusely infiltrating margins of the tumor. Scale bar in (**a**) equals 2.5 mm; scale bar in all SEM images equals 500 nm.

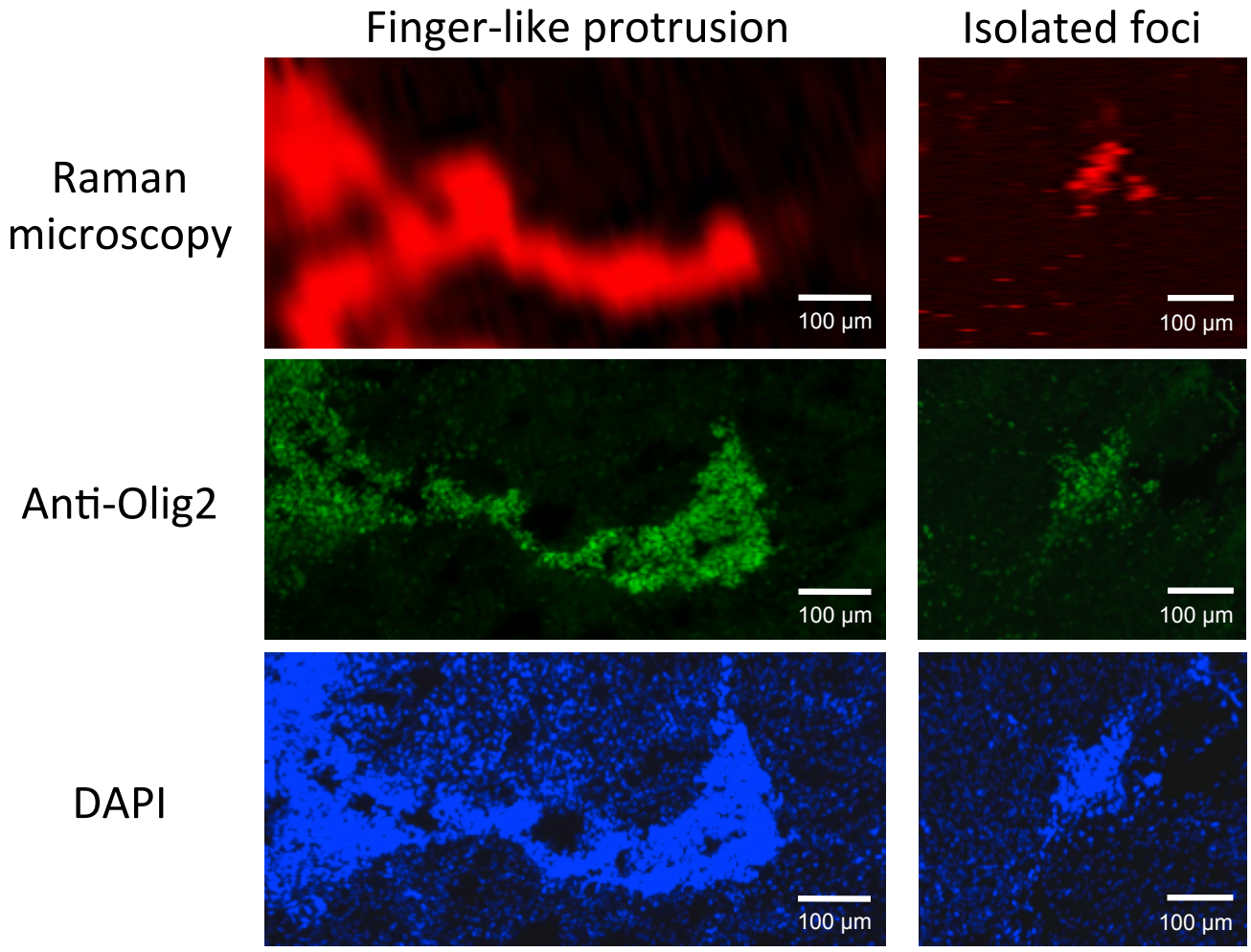

Supplementary Figure 13. MPRs visualize finger-like protrusions and isolated foci in an orthotopic primary human glioblastoma (GBM) xenograft mouse model. Tumor-bearing mice were injected intravenously with MPRs (150 µl, 16 nM, *n* = 4). At 24 h post-injection, brains were excised and cryosections were analyzed with Raman microscopy (500 µm slice thickness) and Olig2-specific immunofluorescent staining of an adjacent section (with DAPI counterstain; 10 µm slice thickness). The Raman signal (red) represents the location of the MPRs, the Olig-2 signal (green) the presence of tumor cells and DAPI (blue) the presence of cellular nuclei of both tumor and surrounding brain (Note that certain differences in co-localization between Raman signal and Olig2/DAPI staining are expected as these images are not taken from the exact same section and volume averaging in the Raman image due to the larger slice thickness can occur). **Left column**: A finger-like tumor protrusion is shown at the edge of the brain tumor. As demonstrated by the good co-localization of the Raman and Olig-2 signal, MPRs accumulated in and were therefore able to outline such a finger-like protrusion. **Right column**: An isolated satellite metastasis away from the main tumor is also depicted by Raman imaging (note the good co-localization of red and green signal). Data is representative of three random slices through each of the four tumors.

Intra-operative Photoacoustic imaging

In addition to the Raman intra-operative experiment (Fig. 5), we have demonstrated that Photoacoustic imaging can further be used to complement Raman imaging in intra-operative guidance of tumor resection. A mouse bearing a glioblastoma tumor (primary human xenograft) was injected with MPRs (150 µl, 16 nM). 24 h post-injection, the mouse was perfused with PBS, sacrificed and the brain excised and embedded in agarose. Photoacoustic images were acquired before and after partial tumor resection (**Supplementary Fig. 14**). An absence of Photoacoustic signal in the resected portion of the tumor was observed, while a residual Photoacoustic signal was observed from the non-resected tumor. This experiment provides preliminary demonstration that the Photoacoustic tomographic information further complements the two-dimensional Raman image, as it provides the surgeon with depth-information on the area that should be resected.

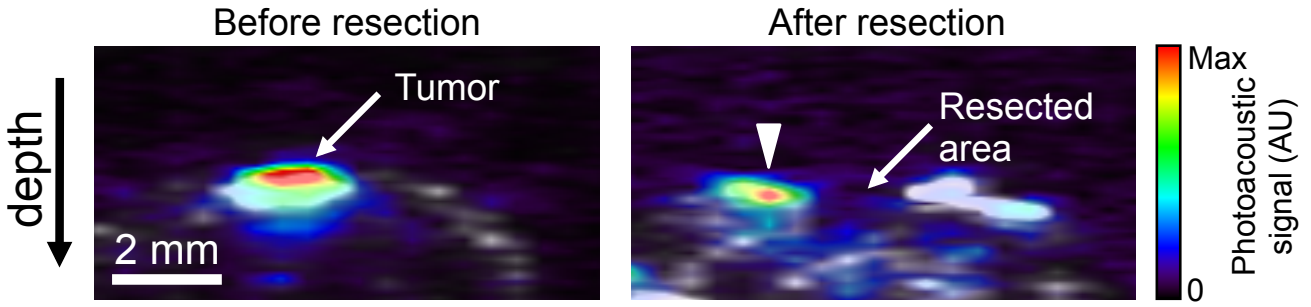

Supplementary Figure 14. Intra-operative Photoacoustic imaging. A mouse bearing a glioblastoma tumor (primary human xenograft) was injected with MPRs (150 µl, 16 nM). After 24 h, the brain was perfused with PBS, excised, and embedded in an agarose gel. Coronal Photoacoustic images were acquired before (left image) and after (right image) partial tumor resection. An absence of Photoacoustic signal in the resected portion of the tumor was observed, while residual Photoacoustic signal (arrow-head) was observed in the area of the non-resected tumor. Note that the increased grayscale ultrasound signal to the right of the resected cavity is likely due the surgical manipulation, an effect that is commonly observed during surgery. Photoacoustic images (color scale from 0 to max) were overlaid on conventional ultrasound images (gray), which outline the gross anatomy of the mouse brain.

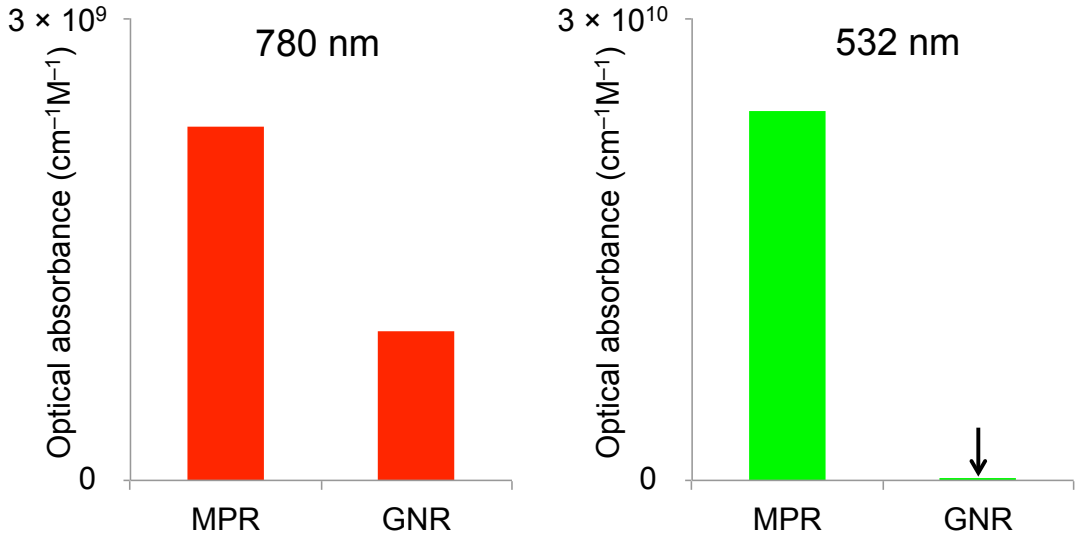

Supplementary Figure 15. Comparison of MPRs to gold nanorods-780 (GNRs) at near-infrared and visible wavelengths. While the absorbance of MPRs is ~2.5-fold higher than GNRs (10 nm diameter, 38 nm length) at 780 nm (red bars), it is 123-fold higher than GNRs at 532 nm (green bars). Data taken from the optical absorbance spectra shown in Figure 2d.

B. Supplementary Discussion

As many disease states do not exhibit an intrinsic Photoacoustic contrast, it is necessary to administer a Photoacoustic contrast agent. The nanoparticle used here with its 60 nm diameter gold core was shown to exhibit the highest Photoacoustic signal reported to our knowledge (e.g., 4,500-fold higher than carbon nanotubes[1] and ~ten-fold higher than most gold nanorods[2]). While other Photoacoustic contrast agents may exhibit lower absolute Photoacoustic signal, some were reported to have peak absorption in the near infra-red[2-5], where tissue background signal is reduced. However, targeting them to tumors has been proven to be highly challenging[2-6]. In fact, apart from this current work, we are not aware of any report where nanoparticles were shown to accumulate in deep tumors and produce a detectable Photoacoustic signal. Hence, while the peak Photoacoustic wavelength of the MPRs is in theory not optimal for tissue penetration, their very high optical absorbance at this wavelength compensates for this fact to some degree (see **Supplementary Figure 15**, showing 123-fold higher absorbance of MPR nanoparticles than gold nanorods (Nanorodz™; Nanopartz Inc., 10 nm diameter, 38 nm length; peak absorbance at 780 nm) at 532 nm and 2.5-fold higher absorbance than gold nanorods at 780 nm). While the exact depth of penetration achievable using the MPRs is not fully known *in vivo*, this parameter could be evaluated in future studies.

Another potential imaging modality that can be leveraged for identifying tumor margins is fluorescence imaging. Compared to Raman or Photoacoustic imaging, fluorescence imaging suffers from a lower sensitivity on the order of 0.5 nM; however, it could be further improved using multispectral imaging analysis[7]. On a per-molar concentration basis, the MPRs exhibit a higher sensitivity compared to fluorescence agents. However, on a per-mass basis, fluorescent dyes may show better sensitivity than Raman imaging, partially due to the relatively large size of the MPRs. Nanoparticles also carry some unique advantages such as a very high EPR effect (i.e., accumulation in tumors) compared to small fluorescent dyes.

High grade gliomas, particularly WHO Grade IV glioma (glioblastoma multiforme), are

characteristically diffuse, grossly hemorrhagic and necrotic. Therefore, establishing a correspondence between pre-operative and intra-operative tumor delineation represents a significant challenge in neuro-oncology and is one that may be overcome with a multimodal imaging agent such as the one described here. A second significant difficulty in tumor resection is the frequent poor definition of the tumor margin, caused by finger-like protrusions of tumor into the adjacent brain parenchyma. Thus, invasive cells may be found to follow small blood vessels (perivascular cuffing), and in myelinated fiber tracts in which cells show intrafascicular, perifascicular, and interfibrillary migration. The detection of such small tumor extensions requires the highest possible sensitivity and resolution. While most studies examining the effect of intra-operative image guidance on survival used MRI and found an associated improved survival due to the more complete resection[8,9], the resolution of clinical MRI does not resolve such small structures. This could represent a reason why the majority of studies using currently available intra-operative imaging methods report a significant increase in length of survival, but are still not able to achieve long-term survival in high-grade gliomas. In our study we have observed that such finger-like protrusions were also detectable by Raman imaging, indicating that this approach may allow more complete resection in these critical areas. Although we have demonstrated the feasibility of the MPR approach in both the U87MG model as well as in an infiltrating human primary xenograft model, a caveat remains that neither of these two models completely recapitulate human brain tumor pathology and thus eventual clinical studies will be needed for further validation.

C. Supplementary Methods

MRI – additional details

For phantom experiments, 50 μL of serial MPR dilutions in MES buffer were placed in customized 384 well plates. For *in vivo* experiments, animals were first anesthetized in a knockdown box with 3% isoflurane. The animals were then placed on a custom-designed MRI-compatible cradle in a 3 cm inner diameter in house quadrature birdcage radio frequency transmit/receive coil and the tube was connected to a ventilator with 1.3-1.5% isoflurane. A fiber-optic temperature probe and respiratory sensor were placed adjacent to the abdomen of the animal. The coil with the animal was inserted to the iso-center of the magnet. Heated air was pumped into the bore to maintain the body temperature of the animals at physiological levels (34-38 °C).

For quantification of tumor enhancement on MRI, the contrast-to-noise ratio (CNR) was used[10]. An axial slice through the middle of the tumor was chosen in the software Osirix. On this slice, an ROI was drawn outlining the margins of the tumor. A second ROI of the same size was placed over brain tissue of the contralateral hemisphere, which did not contain visible tumor. A third ROI was placed outside of the skin near the skull to record image noise. The CNR was then calculated using the following formula: ($signal_{tumor}$ – $signal_{normal\ brain}$)/*standard deviation of noise*[10].

Raman Imaging – additional details

For Raman microscopy, frozen sections were placed on quartz slides (Ted Pella, Inc.) and air-dried. A greater slice thickness (50 μm or 500 μm, depending on the purpose of the experiment) than for immunohistochemistry was chosen in order to increase Raman signal intensity. A 5x or 12x lens was used, and Raman spectral maps and correlating white light images were acquired using the Renishaw Streamline™ function. Spectra were analyzed by least squares analysis using Wire 2.0 Software (Renishaw).

Photoacoustic Imaging – additional details

A precision xyz-stage (U500, Aerotech Inc.) with a minimum step size of 1 μm was used to move the transducer and the fiber ring along a planar 2D trajectory. At every position, the acquired signal was averaged over 2 to 4 laser pulses. The time of arrival and the intensity of the laser pulses were recorded using a silicon photodiode (DET10A, Thorlabs). This information was used to synchronize the acquisition and compensate for pulse-to-pulse variations in laser intensity. The analog Photoacoustic signals were amplified using a 30 dB preamplifier (5676/115VAC, Panametrics-Olympus NDT) and digitized using an oscilloscope (Infiniium 54825A, Agilent). The Photoacoustic and ultrasound images were reconstructed as follows: the a-scan from each position of the transducer was band pass filtered with 100% fractional bandwidth, compensated for laser intensity variations and envelope detected. The a-scans were then combined to reconstruct a 3D intensity image of the target. No further post-processing was done on the images. The ultrasound images were acquired using a 5 or 25 MHz transducer.

Photoacoustic-MRI and Raman-MRI co-registration and 3D visualization

Since the Photoacoustic image is intrinsically three-dimensional, we co-registered it to the MRI image and rendered their overlay in 3D. A conventional ultrasound image was taken with the same transducer that was used to acquire the Photoacoustic image, thereby producing perfectly co-registered Photoacoustic and ultrasound images. The ultrasound image highlighted the mouse brain anatomy such as skull curvature, which then allowed us to manually find the exact rigid-body alignment needed to register the ultrasound image to the MRI image. We then applied the same rigid-body alignment to the Photoacoustic image. The 3D rendering of the two images was done in the commercial software Amira™ (Visage Imaging, Inc.). The Raman images were acquired using precise topographical landmarks of the mouse anatomy. The Raman image with its known dimensions and matrix size and the MRI data were then manually co-registered based on these landmarks and the known size and position of the acquired images.

Histology

Brain tissue was embedded in optimal cutting temperature material (O.C.T.; Sakura) and snap-frozen in liquid nitrogen. Frozen sections (10 μm slice thickness) were obtained using a cryotome (Leica). For Raman microscopy, 50 μm or 500 μm sections were cut immediately adjacent to a slice used for immunohistochemistry.

Slides were air-dried for 2 h at RT, then fixed in cold acetone for 5 min and air dried for 1 h. Slides were then washed for 5 min in PBS to remove the O.C.T.. Samples were then stained with Rat anti-CD11b (BD Pharmingen, dilution 1:100) for 2 h at RT, Goat anti-Rat-biotinylated (Jackson ImmunoResearch, dilution 1:500) for 30 min at RT, StreptAvidin-AlexaFluor 594 (Invitrogen, dilution 1:300) for 30 min at RT, and Rabbit anti-GFP-AlexaFluor 488 (Invitrogen, dilution 1:500) for 1 h at RT. Slides were counterstained with DAPI for 3 min.

For Olig-2/CD68 double staining, sections were air-dried for 2 h at RT, then fixed in 4% paraformaldehyde in PBS for 10 min and rehydrated by an ethanol gradient wash. After two washes in PBS and permeabilization in 0.3% Triton in PBS for 30 min, sections were incubated in PBS containing 2% BSA, 5% NDS, 0.1% Triton for 1 h at RT, followed by anti-CD68 (1:1000; Serotec) over night at 4°C. After 3 washes with PBS/0.1% Triton sections were incubated with Alexa Fluor 488 donkey anti-rat IgG (H+L) (Invitrogen, dilution 1:500) for 1 h at RT. After washes in PBS/0.1% Triton and blocking in PBS containing 2% BSA, 5% NDS, 0.1% Triton for 20 min at RT, the sections were incubated for 2 h at RT with anti-Olig2 (1:250, Chemicon #9610) followed by PBS/0.1% Triton washes and after 3 washes with PBS/0.1% Triton sections were incubated with Alexa Fluor 555 donkey anti-rabbit IgG (H+L) (Invitrogen, dilution 1:500). After secondary antibody staining, sections were washed with PBS/0.1% Triton and counterstained with DAPI. Samples were examined using a TCS SP2 AOBS (Leica) Confocal Laser Scanning Microscope or DMI6000 inverted fluorescence microscope (Leica).

Statistical Methods

Correlation of signal increase with increasing concentration *in vitro* was tested with mixed effects linear regression of $\log_{10}$ signal ratio to baseline on $\log_{10}$ concentration, imaging method, and their interaction, with individual phantom area as the random factor. Correlation of signal increase with increasing concentration in living mice, and differences in rate of signal increase between imaging methods in living mice were tested with mixed effects linear regression of $\log_{10}$ signal ratio to baseline on $\log_{10}$ concentration, imaging method, and their interaction, with mouse as the random factor. The MPR tumor targeting experiments were analyzed via one-sided t-test, where MRI and Photoacoustic post-injection measurements were compared against a ratio of 1 with a one-sided one-sample t-test, and Raman post-injection measurements were compared against an average noise value of 0.001 with a one-sided one-sample t-test. The MPR tumor targeting kinetics study initial increase was tested with one-sided student's t-test. The signals were then re-expressed as log of ratio to pre-injection baseline. Differences between imaging methods in time course of signal from 30–120 min were tested with mixed effects linear regression of $\log_{10}$ signal ratio to baseline on $\log_{10}$ concentration, imaging method, and their interaction, with mouse as the random factor.

Mouse arrangement in the Photoacoustic system

Female nude mice were used for all the Photoacoustic studies. The mice that were scanned in the Photoacoustic system were fully anesthetized using isoflurane delivered through a nose-cone. Prior to the Photoacoustic scan, the head of the mouse was slightly tilted to expose the right lobe to the imaging system. The head was then covered by Gonak gel (Akorn) and covered by a saran-wrap water bath. The ultrasonic transducer in the water bath was therefore acoustically coupled to the mouse brain tissues. This setup allowed the ultrasonic transducer to move freely in 3D while applying only minimal physical pressure on the mouse head (**Supplementary Figure 16**).

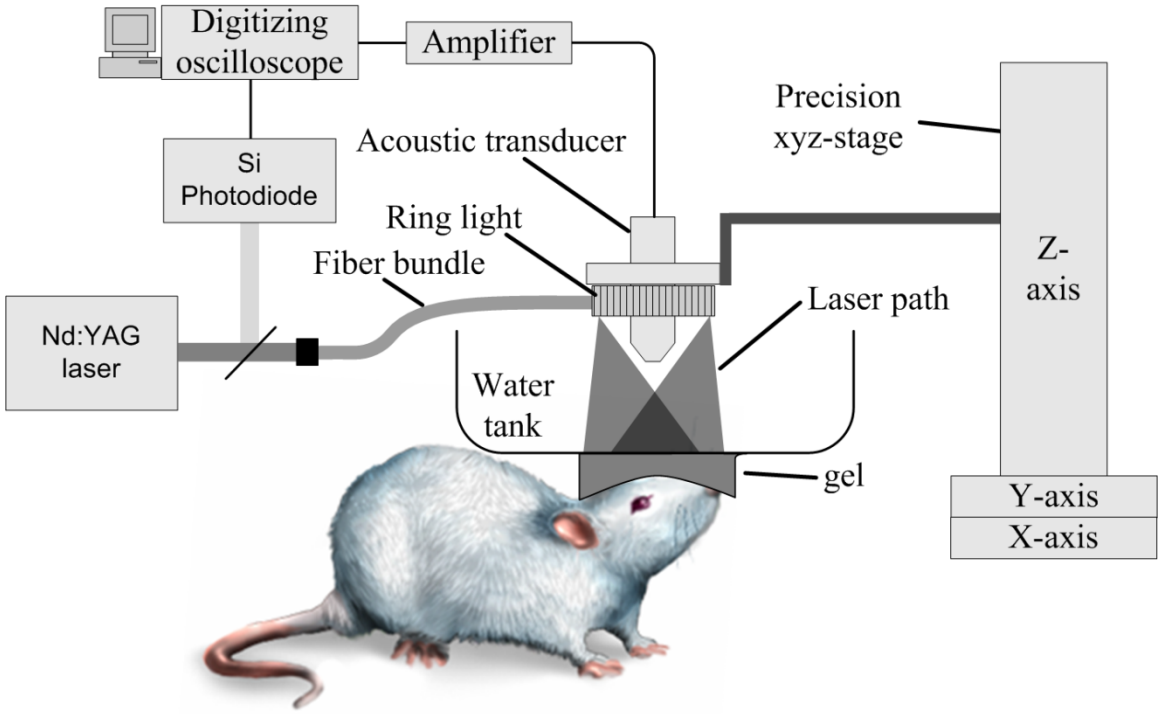

Supplementary Figure 16: Photoacoustic imaging instrument. A tunable pulsed laser (Nd:YAG laser) illuminated the subject through a fiber optic ring light. The Photoacoustic signals produced by the sample were acquired using either a 5 MHz or 25 MHz focused transducer. A precision xyz-stage was used to move the transducer and the fiber ring along a planar 2D trajectory. The time of arrival and the intensity of the laser pulses were recorded using a silicon photodiode. This information was used to synchronize the acquisition and compensate for pulse-to-pulse variations in laser intensity. The analog Photoacoustic signal was amplified using a 30 dB preamplifier and digitized using an oscilloscope.

Stereotactic brain tumor implantation

All aspects of experimental manipulation were in strict accord with guidelines from the National Institute of Health and have been approved by members of the Stanford Institutional Animal Care and Use Committee (IACUC). Ten week old female nude mice (Charles River), or five week old male SCID mice (Taconic Farms, Inc.), respectively, were anesthetized using 2.0% isoflurane and positioned in a Benchmark® (Leica) stereotactic instrument (**Supplementary Figure 17**).

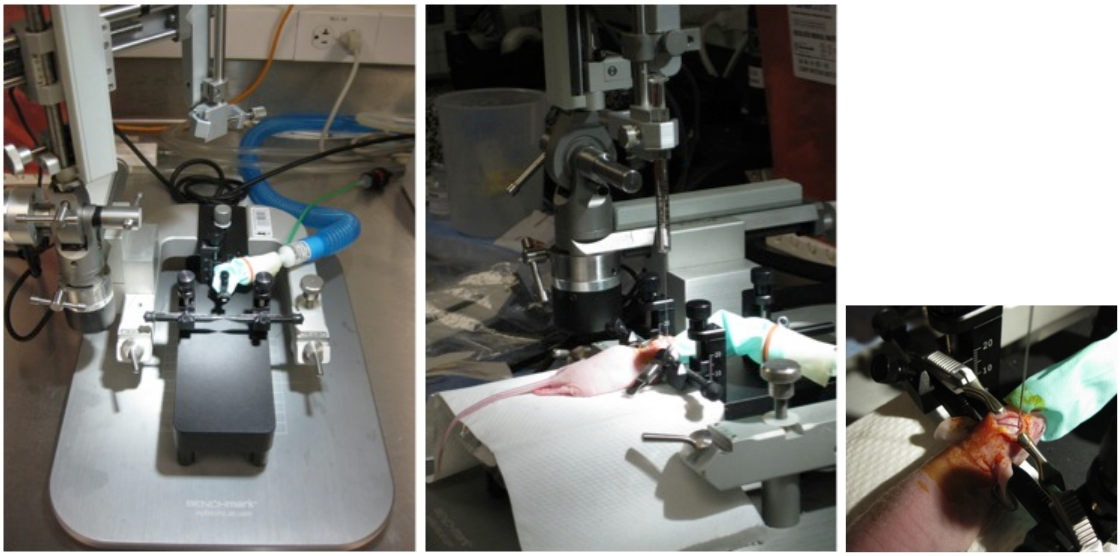

Supplementary Figure 17. Stereotactic brain tumor implantation.

Mice also received a subcutaneous injection of 0.1 mL of a 1:10 dilution of 0.3 mg/mL buprenorphine as additional anesthesia. The top of the animal's head was cleaned with 70% ethanol and betadine. Ophthalmic ointment was applied, a linear skin incision was made over the bregma, and 3% hydrogen peroxide was applied to the periost with a cotton swab. A 27G needle was then used to drill a burrhole into the skull 0.5 mm anterior and 2 mm lateral to the bregma. A 10 μL gas-tight syringe (Hamilton) was then used to inject 2 μL of the eGFP^{+}U87MG-cell suspension or TS543 human glioblastoma cells (3 x 10^{5} cells in PBS) in the striatum at a depth of 2.5 mm from the dural surface. TS543 is a glioblastoma multiforme cell line derived from a human glioblastoma and propagated as tumor

spheres in NeuroCult media (STEMCELL Technologies). The injection was done slowly over 10 min. The burrhole was occluded with glue to prevent leakage of cerebrospinal fluid, and the skin was closed with surgical clips. Animals were used for experiments after 3-5 weeks, when tumors had reached a size of approximately 5 mm diameter as determined by MRI.

Optical and Raman photobleaching studies

We tested the optical stability of the MPRs under increasing durations of light exposure (photobleaching). For assessment of photobleaching by the Photoacoustic laser, the sample was continuously exposed over 30 min (532 nm, power density of 8 mJ/cm^2, 10 Hz repetition rate) which were the wavelength and power settings used in our animal experiments.

For assessment of photobleaching by the Raman laser, a 20 μL sample of MPRs in MES buffer was placed in a cell-counting slide. The sample was then continuously exposed to the Raman excitation laser (785 nm) and the Raman signal was recorded every 30 seconds.

Signal linearity phantom study

To test the linearity of the Photoacoustic signal as a function of MPR concentration, we used an agarose phantom with no scattering or absorbing additives. MPRs at increasing concentrations were mixed with warm liquid agarose (n = 3 samples for each concentration) forming MPR solutions at 0, 1.2, 2.4, 4.9, 9.8, 19, 39, 78, 156, 312, 625 and 1250 pM (additional concentrations for Raman imaging included concentrations of 300 and 610 fM). Inclusions 2-3 mm deep were made in the agarose phantom and ~100 µL of MPR/agarose solution was poured into the well. Upon solidification of the gel, another layer of ~3 mm of liquid agarose was poured on top of the phantom. A complete 532 nm Photoacoustic image of the phantom was acquired with a step size of 0.25 mm. Three-dimensional cylindrical ROIs of the size of the inclusion were used to estimate the Photoacoustic signal from each well. Subsequently, a Raman image of the phantom was acquired using a 1 mm step size and 1 s integration time. The 2D Raman image was analyzed by ROI analysis using ROIs encompassing the inclusions. Finally, a T1-weighted MR image of the phantom was acquired. Due to the large size of the phantom compared to the RF coil used, and in order to preserve homogeneity of the RF fields across the phantom, the phantom was scanned in two parts, which were later combined together into one image. Two-dimensional ROIs encompassing the inclusions were placed on a slice through the middle of the inclusion using Osirix imaging software. The signal intensity expressed in arbitrary units for each of the three modalities represents the mean from each of the triplicate wells.

MPR detection and sensitivity in living mice

Solutions of MPRs at different concentrations were mixed with matrigel (Matrigel Basement Membrane Matrix, Phenol Red-free, Becton Dickinson) at 1:1 ratio creating MPR solutions at 50, 100, 200, 400, 800 and 1100 pM. The solutions were then injected subcutaneously (50 μL) to the lower back of mice (n = 3). After solidification of the matrigel, the back of the mouse was scanned with the MRI, Photoacoustic and Raman imaging systems. The Photoacoustic image was taken with lateral step size of 0.25 mm using a 5 MHz transducer at a wavelength of 532 nm. Following the Photoacoustic scan, an ultrasound image was acquired using the same 5 MHz transducer and the two images were then overlaid one on top of the other using AMIDE software[11]. Quantification of the Photoacoustic signal was done by drawing a 3D ROI over the inclusion volume that was visualized in the ultrasound image. The Raman image was taken with a lateral step size of 750 μm and an integration time of 1 s. ROI analysis was performed on the 2D Raman image using circular ROIs. T1-weighted fast spin echo MR images were obtained with parameters described before (see Methods). 2D ROIs encompassing the inclusions were placed within a slice through the middle of the inclusion using the software Osirix. The signal intensity expressed in arbitrary units for each of the three modalities represents the mean for each of the three mice.

Quantitative Raman spectral analysis

The direct classical least squares (DCLS) method was used in this work to perform quantitative analysis of Raman spectroscopy[12,13]. DCLS finds the linear combination of spectra from the MPR Raman signal contained in the area of interest (brain) that most closely matches the Raman spectrum of the MPRs injected intravenously. The pure component spectrum of the MPRs that contains the Raman-active organic molecule, trans-1,2-bis(4-pyridyl)-ethylene, was acquired from a pure 3 mL sample aliquotted onto a quartz slide under the microscope. The multiplicative constants derived by the DCLS analysis are proportional to the concentration of the pure components. Before injection and scanning, a pure spectra component was taken from the MPRs along with the mouse Raman background signal that was used as a background component (which was later subtracted). The DCLS method gave very accurate results since the pure spectral component remained consistent throughout the analysis. The quantitative data shown was analyzed based on the Raman maps acquired from each mouse at various time points. A region of interest was drawn around the tumor area and an average accumulation of nanoparticles was estimated in that region based on the pure spectral component of the MPRs, as described above. For some experiments, such as photobleaching studies, Raman spectra from a single point over the sample of interest were analyzed.

Scanning Transmission Electron Microscopy of tissue samples

Tissue samples from both healthy brain and tumor were fixed in a solution of 4% paraformaldehyde in 0.1 M sodium cacodylate buffer. Samples were then stained with 1% osmium tetroxide in water at 4ºC for 2 h. After 2 h, the tissue samples were rinsed with deionized water and stained with 1% uranyl acetate at 4ºC overnight. Samples were then dehydrated in progressively higher concentrations of ethanol at 4ºC; 50%, 70%, and 95%. The tissue samples were then allowed to gradually warm to RT. Samples were further dehydrated 2x in 100% ethanol and 3x in propylene oxide. Samples were then embedded in Embed 812 epoxy resin (EMSdiasum). Samples were placed in 1:1 solution of Embed 812:propylene oxide for 1 h at RT. Samples were then placed in 2:1 solution of Embed 812:propylene

oxide overnight. Finally samples were placed in 100% Embed 812 for 1 h before being placed in molds and cured overnight at 60ºC. Thin sections (150 nm) were then cut from the tissue samples using an Ultracut S microtome (Leica) and placed on 200 mesh bare copper grids. The sections were examined without coverslip using a Tecnai G2 X-Twin (FEI) scanning transmission electron microscope (STEM) operating at 120 kV in scanning mode.

Scanning Electron Microscopy of tissue samples

Images of histology slides of brain tissue stained with hematoxylin and eosin were acquired using a DM 2000 light microscope (Leica). Images were taken and stitched together to create a large composite image of the entire brain section. The histology slides were then coated with a thin AuPd film to improve conductivity and placed in a XHR scanning electron microscope (SEM) (Magellan). The SEM was operated at 15 kV with a probe current of 50 pA. Both secondary electron and backscattered electron images were collected. Backscattered electron imaging was utilized to locate the MPRs in the brain tissue.

Inductively coupled plasma atomic emission spectroscopy (ICP-AES)

An aliquot of 385 μL of 3.86 nM MPR suspension was washed 2x in water and then pelleted by centrifugation. The pellet was re-suspended in 2 mL of 10 M of sodium hydroxide and sonicated for 10 min in a sonication bath at RT. This was followed by slow addition of 70% HNO_3 until the pH became acidic. The volume of the resulted mixture was brought to 10 mL and analyzed for the presence of Gd^{+3} ions using an IRIS Advantage/1000 Radial ICAP Spectrometer (Thermo Scientific).

Tissue-mimicking phantom for comparing depth of penetration of Photoacoustic versus Raman imaging

The phantom was based on a 1% agarose mixed with India Ink to mimic tissue absorption (to make the final agarose-solution at optical absorbance of 1.0 cm^{-1}) and Liposyn 0.5% to mimic tissue scattering. The agarose liquid was left to solidify in a plastic container that was slightly tilted. As the agarose solidified, small inclusions of ~3 mm diameter and 1-2 mm in depth were made using a small pipette tip. MPRs mixed in liquid agarose-solution at 1 nM concentration were embedded in the small inclusions. As the inclusions solidified, the plastic container was positioned on a flat surface and an additional layer of agarose-solution was poured on the phantom to seal it.

References for Supplementary Information

1. de la Zerda, A.*, et al.* Carbon nanotubes as photoacoustic molecular imaging agents in living mice. *Nat Nanotechnol* **3**, 557-562 (2008).
2. Eghtedari, M.*, et al.* High sensitivity of in vivo detection of gold nanorods using a laser optoacoustic imaging system. *Nano Lett.* **7**, 1914-1918 (2007).
3. Razansky, D.*, et al.* Multispectral opto-acoustic tomography of deep-seated fluorescent proteins in vivo. *Nat Photon* **3**, 412-417 (2009).
4. Kim, J.W., Galanzha, E.I., Shashkov, E.V., Moon, H.M. & Zharov, V.P. Golden carbon nanotubes as multimodal photoacoustic and photothermal high-contrast molecular agents. *Nat Nanotechnol* **4**, 688-694 (2009).
5. Kim, G.*, et al.* Indocyanine-green-embedded PEBBLEs as a contrast agent for photoacoustic imaging. *J. Biomed. Opt.* **12**, 044020 (2007).
6. Agarwal, A.*, et al.* Targeted gold nanorod contrast agent for prostate cancer detection by photoacoustic imaging. *J. Appl. Phys.* **102**, 064701-064704 (2007).
7. Mansfield, J.R., Gossage, K.W., Hoyt, C.C. & Levenson, R.M. Autofluorescence removal, multiplexing, and automated analysis methods for in-vivo fluorescence imaging. *Journal of biomedical optics* **10**, 41207 (2005).
8. Schneider, J.P.*, et al.* Intraoperative MRI to guide the resection of primary supratentorial glioblastoma multiforme--a quantitative radiological analysis. *Neuroradiology* **47**, 489-500 (2005).
9. Senft, C.*, et al.* Influence of iMRI-guidance on the extent of resection and survival of patients with glioblastoma multiforme. *Technol Cancer Res Treat* **9**, 339-346 (2010).
10. Bushberg, J.T., Seibert., J.A., Leidholdt, E.M. & Boone, J.M. *Essential Physics of Medical Imaging*, (Lippincott Williams & Wilkins, 2001).
11. Loening, A.M. & Gambhir, S.S. AMIDE: a free software tool for multimodality medical image analysis. *Mol. Imaging* **2**, 131-137 (2003).
12. Haaland, D.M. & Easterling, R.G. Improved Sensitivity of Infrared Spectroscopy by the Application of Least Squares Methods. *Appl Spec* **34**, 539-548 (1980).
13. Pelletier, M.J. Quantitative Analysis Using Raman Spectroscopy. *Appl Spect* **57**, 20A-42A (2003).